BNL-91097-2010-CRAD

FINAL REPORT

FOR CRADA NO. C-06-12

BETWEEN

BROOKHAVEN SCIENCE ASSOCIATES

AND

AMERICAN SUPERCONDUCTOR

Project Entitled: Study of the Nucleation and Growth of YBCO on Oxide Buffered Metallic Tapes

Brookhaven PI: Vyacheslav Solovyov

Submitted by: Michael J. Furey
Manager, Research Partnerships
Brookhaven National Laboratory

DISCLAIMER

FINAL REPORT

FOR CRADA NO. C-06-12

BETWEEN

BROOKHAVEN SCIENCE ASSOCIATES

AND

AMERICAN SUPERCONDUCTOR

Project Entitled: Study of the Nucleation and Growth of YBCO on Oxide Buffered Metallic Tapes

Brookhaven PI: Vyacheslav Solovyov

Submitted by: Michael J. Furey
Manager, Research Partnerships
Brookhaven National Laboratory

DISCLAIMER

Final report on CRADA: Study of the nucleation and growth of YBCO on oxide buffered metallic tapes

TECHNOLOGY AREA: Materials

BROOKHAVEN PI(s):

Dr. Vyacheslav Solovyov,

Associate Scientist,

Department of Condensed Matter Physics and Materials Science,

Building 480,

Tel: 631-344-5437

e-mail: solov@bnl.gov.

INDUSTRY PARTICIPANT: American Superconductor Inc.

Two Technology Drive

Westborough, MA, 01581-1727

INDUSTRY PARTICIPANT P.I.:

Dr. Martin Rupich,

Senior Scientist,

American Superconductor Inc.

Two Technology Drive

Westborough, MA, 01581-1727

Tel: (508) 836-4200

e-mail: mrupich@amsuper.com

Final report on CRADA: Study of the nucleation and growth of YBCO on oxide buffered metallic tapes

Table of Contents

Final report on CRADA: Study of the nucleation and growth of YBCO on oxide buffered metallic tapes

1. Technical report CRADA work

1.1. CRADA objectives

The CRADA collaboration will concentrate on developing the scientific understanding of the factors necessary for commercialization of high temperature superconductors (HTS) based on the YBCO coated conductor technology for electric power applications. The project will pursue the following objectives:

1. Establish the correlations between the YBCO nuclei density and the properties of the CeO_2 layer of the RABiTS^{TM} template.
2. Compare the nucleation and growth of e-beam and MOD based precursors on the buffered RABiTS^{TM} templates and clarify the materials science behind the difference.
3. Explore routes for the optimization of the nucleation and growth of thick film MOD precursors in order to achieve high critical current densities in thick films.

1.2. Background

Recent improvements in the second-generation (2G) high-temperature superconductor technology, such as control of substrate texture and introduction of novel pinning strategies [1-5] raised critical current densities to above 1000 A/cm [6], which is a target value for many applications. As the 2G wires are entering the market place, reproducibility and cost of long-length 2G wire production need to be better optimized. Since 2G wire technology is a scaled-up epitaxial process, the nucleation of the epitaxial phase on the substrate is a critical step. The unique challenge is to realize a robust nucleation of c-axis oriented YBCO on inexpensive substrates that are several kilometers long, using a fast, economical deposition process. This requires a coordinated effort in two areas: (i) optimization of processing parameters to achieve the maximum performance and (ii) engineering the substrate to expand the optimum processing window and make the process more robust.

The metal-organic deposition (MOD) process is gaining popularity as an inexpensive way to grow YBCO layers over 1 μm thick, with excellent superconducting properties [7-9]. This method is used by AMSC for 2G wire production, therefore it was chosen as a primary synthetic route. MOD processing starts with deposition of fluorinated metal-organic precursor a buffered metal tape, such as RABiTS. After a few minutes of processing, YBCO nuclei form on the precursor-substrate interface [10-11]. It is well known that by careful adjustment of the processing conditions, such as the processing atmosphere composition [12-13], the growth rate [14-15], and the precursor state [16-18], one can maximize c-axis oriented nucleation while keeping random and c-axis orientation to a minimum. This optimization approach has limits. The window of optimum processing may be too narrow to be reliably satisfied and the maximum achievable J_c value is often low, especially for thicker precursor layers [19]. Another complication is that it is difficult to maintain uniform processing conditions in a large-scale

reactor. This emphasizes important role of the substrate engineering as a way to make large-scale processing more robust. The traditional science of epitaxial nucleation deals with single crystal substrates. Fig. 1A is an artistic rendering of island (Vollmer-Weber) nucleation on a single-crystalline wafer. A typical single crystal surface consists of (001) terraces terminated by vicinal steps. Depending on growth conditions, nuclei of the epitaxial phase attach either to the vicinal steps or the terraces, which opens many possibilities for guiding the nucleation in the desired direction. In contrast, the surface of an oxide buffer has a completely different morphology. It is comprised of small grains (<100 nm lateral grain size) with short (001) terminations void of the vicinal steps, Fig. 1B. Therefore, a new growth optimization and substrate engineering approach may be required for an oxide buffer as opposed to the case of a single-crystal wafer.

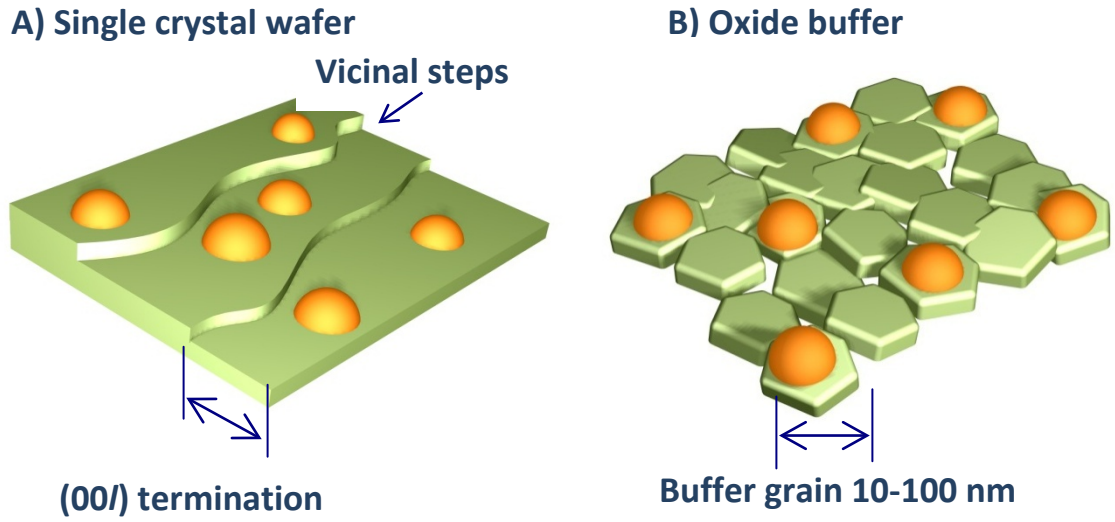

Fig. 1. Vollmer-Weber nucleation on a single-crystalline (001) surface and (001) textured oxide buffer. In a single crystal, 1- 0.1 μm (001) terraces and vicinal steps dominate the surface landscape. In contrast, a thin oxide buffer is comprised of small, 10-100 nm, grains with short (001) terminations.

Cerium oxide is currently the substrate buffer of choice for 2G wire production by MOD method. Cerium oxide films find various applications as a catalyst [20-22], template layer for epitaxial growth of complex oxides, and a diffusion barrier. In many applications, CeO2 is deposited as a thin (<0.1 um) epitaxial layer on an appropriate substrate. If a (001) film is used as an epitaxial template, it is desirable to have a film with well-defined (001) surface termination. For example, (001)-oriented ceria layer is now widely used as a template for growth of a thick oriented layer of high-temperature superconductor, Y1Ba2Cu3O7, which is a

Final report on CRADA: Study of the nucleation and growth of YBCO on oxide buffered metallic tapes

critical component of the so-called second-generation superconducting wires developed by our industrial CRADA participant, American Superconductor Corporation. A template with low density or small (001) terminations would provide a low density of nucleation sites for the Y1Ba2Cu3O7 phase. As a consequence, other undesirable phases would be allowed to nucleate, reducing the structural quality of the film.[23]

The atom arrangement on (001) face of ceria is such that the surface energy is approximately two times higher than the other low-index faces: (111) and (110). The high energy of the (001) face has been theoretically explained by weak bonding of the O^{2-} ion to (100) surface,[24],[25] which has been confirmed experimentally.[26] Given the difference in surface energies of low-index faces, a Wulff construction[27-28] predicts that at equilibrium a ceria crystal would take the shape of a truncated octahedron with (111) planes being the primary terminations and (001) planes truncating the octahedron vertices.[29] A Wulff construction becomes inaccurate on the nano-scale level, because the atomistic nature of crystal faces starts to play a significant role in the energy balance and packing corrections have to be introduced. Corrected Wulff plots for 10^4-10^9 atom clusters of a model cubic material were calculated by Marks;[30] it was shown that the surface fraction of (001) terminations gradually disappears as the cluster became smaller than 10^6 atoms. Indeed, it was observed that unsupported ceria particles less than 10 nm in diameter were (111) terminated octahedra with no (001) truncations.[31] The tendency for (111) termination of small ceria grain was also recognized in epitaxial (001) films: in films with small lateral grain size the surface was comprised of pyramid-like (111) facets.[32],[33] Contrast between (100) and (111) ceria orientations has been emphasized by Wu et al.,[33] who compared CeO_2 epitaxy on (001) and (111) faces of yttria-stabilized zirconia (YSZ) single crystals. Films deposited on (111) YSZ face exhibited excellent flatness and crystallinity, while (001)-oriented films deposited under the same conditions on (001) YSZ face were invariably small-grained and rough.

The CRADA work proceeded in two steps:

1. Detailed characterization of epitaxial ceria layers on “model” substrates, such as (001) YSZ and on RABiTS tapes.

2. Study of YBCO nucleation on well-defined substrates and on long-length RABiTS.

1.3. Project description

a. Characterization of (001) ceria buffers using X-ray radiation facilities and Center for Functional Nanomaterials and National Synchrotron Light Source.

In this part of the CRADA work we use X-ray reciprocal-space mapping to explore the dynamics of lateral grain growth in CeO_2 films deposited on r-cut sapphire and (001) YSZ. Mapping of (*hkl*) reflections allow us to acquire reliable averaged information about grain structure and strain magnitude and arrive at a consistent quantitative description of the lateral structure. The work complements earlier microscopy studies of similar samples.[32, 34] The goal is to understand

how one can synthesize ceria, and possibly other refractory oxide films, with large grains with well-defined (001) terminations.

Cerium oxide films were deposited using a large-area pulsed laser deposition system. The films were deposited on r-cut sapphire and (001) YSZ at two substrate temperatures, 700 and 650 ^{o}C. The system was equipped with a KrF excimer laser source (248 nm wavelength, Lambda Physik Compex LPX 305i) operated at a repetition rate of 10 Hz and pulse energy of 600mJ, which yielded an average deposition rate of ~0.5 nm/min. The processing atmosphere consisted of 175 mTorr partial pressure of oxygen. After deposition the samples were annealed in air at 1050 ^{o}C for periods of time ranging from 10 min to 2 hr.[35] The sample surface roughness was analyzed by atomic force microscopy in ambient atmosphere using Asylum Research MFP-3D-BIO atomic force microscope (AFM).

X-ray reciprocal-space mapping was chosen as a primary method for determining the lateral structure of these films. Fig. 2 shows approximate locations of the reflections used in this work with respect to the film surface and directions of three principal scans: 2θ, ϕ and ω. Each reflection is a three-dimensional object occupying a part of reciprocal space centered at the location given by the Bragg diffraction condition $|\mathbf{S}| = 2\sin(\theta)/\lambda$, where θ is the reflection Bragg scattering vector **S** pointing at the reflection maximum. The reciprocal space mapping can be described as sectioning of a three-dimensional reflection by a plane in reciprocal space. Two planes are commonly used for the purpose: 2θ–ω plane, normal to the film surface and containing **S** vector, and ϕ–ω plane, normal to the **S** vector, as shown in Fig. 2. During ϕ–ω, or "pole figure" scan, a reflection is sectioned by the ϕ–ω plane; this provides information on the film texture. Combination of 2θ–ω scans and mapping the reflection in 2θ–ω plane allows separating normal and lateral strain and size broadening effects. In this work we present maps which are sections of ceria reflections by 2θ–ω plane.

In an epitaxial (00*l*) ceria film only (002) and (004) peaks can be accessed in the symmetric scattering geometry, i.e. when the scattering vector **S** is normal to the film surface. More information can be accessed from mapping asymmetric (*hkl*) reflections with the **S** vector tilted at an angle ψ with respect to the film normal, Fig. 2. These reflections are important since the scattering vector **S** has non-zero lateral component S_x, thus providing insight on the lateral strain of the film. We have selected three reflections with significantly different inclination angles: (002), $\psi = 0^{o}$; (004) $\psi = 0^{o}$; (115), $\psi = 15^{o}$; (224), $\psi = 35^{o}$. Mapping these reflections gives a relatively complete picture of the average film structure in both lateral and normal directions. Additionally, during the scans both incident and reflected beams stay in a plane defined by [001] and [110] directions. The constant instrument geometry with no in-plane rotation allows for quantitative comparison of maps of different reflections and assures that the instrument function stays constant. In the following we denote the **X** direction as one parallel to [110] of the CeO_2 layer and the **Z** direction as one parallel to [001]. Fig. 2 also shows two sources of the reflection broadening: the film thickness and the lateral grain size were responsible for the reflections broadening in the **Z** and **X** directions respectively.

Final report on CRADA: Study of the nucleation and growth of YBCO on oxide buffered metallic tapes

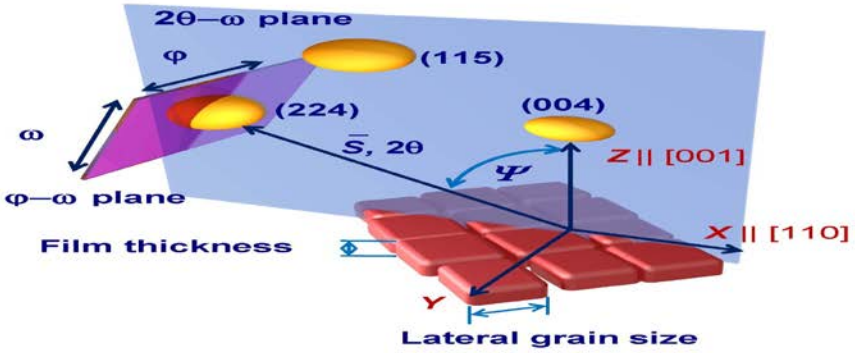

Fig. 2. Schematic view of the X-ray reciprocal mapping geometry, used in the CRADA work, showing the scattering vector S, the coordinate axes, and directions of the principal scans: ϕ, ω and 2θ. Three reflections (004), (115) and (224), shown as ellipsoids, were mapped in a plane defined by [001] and [110] directions. The maps presented in this work are sections of a reflection by 2θ–ω plane. The lateral grain size and the film thickness are shown as the major contributors to the reflection broadening.

Fig. 3 demonstrates the evolution of deconvoluted reciprocal space maps (RSM) for two extreme cases: (i) a large-grained sample, 20 nm thick ceria film on r-cut sapphire deposited at 700 ^{o}C, Fig. 3A, and annealed for 1 hr at 1050 ^{o}C, Fig. 3B; (ii) a small-grained sample, 20 nm thick ceria film deposited at 650 ^{o}C on (001) YSZ, Fig. 3C, and annealed for 1 hr at 1050 C^{o}, Fig. 3D. The maps are aligned vertically from the symmetric (004) reflection with zero inclination angle followed by skewed (115), ψ =15.4^{o} and (224) ψ = 34.5^{o} reflections. A film deposited at 700 ^{o}C on r-cut sapphire has a fairly large initial grain size, as indicated by the narrow resolution limited (004) reflection, Fig. 3A, however the Bragg peak is surrounded by a diffuse scattering tail. Upon examining the maps we notice that Bragg peaks become broader as we move from the symmetric (004) reflection with S_x = 0 nm^{-1} to reflections with non-zero S_x, (115) and (224). On the other hand, the Bragg peaks width in the **Z** direction remains practically unchanged for all the three maps. Fig. 3B shows the effect of 1 hr annealing at 1050 ^{o}C in air on the same set of RSM's. In these samples the RSM shape is dominated by lateral inhomogeneous (RMS) strain which causes lateral broadening of tilted reflections (115) and (224) with non-zero lateral

scattering vector component S_x. The normal direction broadening stayed constant as S_z changed, indicating the low normal strain of the film, as shown by dotted lines in Fig. 3B.

Fig. 3C and D reflect change of the microstructure of the 20 nm CeO_2 film deposited at 650 ^oC on (001) YSZ substrate. This figure is an illustration of a map set for a very small-grained sample: the as-deposited sample has columnar grain morphology with the lateral grain size smaller than the film thickness, which is indicated by the elliptical shape of the maps. By measuring the integral half-width of the Bragg reflection one can easily infer from maps in Fig. 3C that the as-deposited sample was comprised of 20-nm-long and 10-nm-wide columnar grains. After the annealing we observed lateral grain growth and reduction of the lateral RMS strain, as demonstrated by narrower lateral reflections of the annealed sample, Fig. 3D, the lateral grain size approximately doubled after 1 hr annealing. Due to proximity of very strong YSZ substrate reflections, the (004) and (224) maps contained a trace of the YSZ peak visible as a rod in the upper half of the map. This is a typical situation we encountered in CeO_2 on YSZ system: the grain growth saturated after approximately doubling the initial grain size.

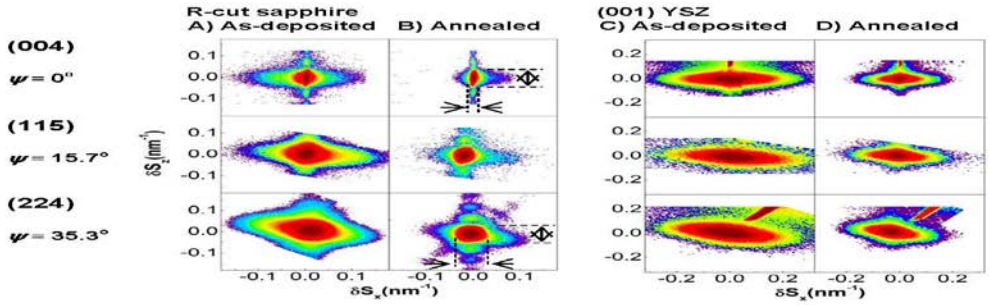

Fig. 3. Reciprocal space maps of (004), (115) and (224) reflections of a 20 nm (001) oriented CeO2 buffers on r-cut sapphire and (001) YSZ: A) as deposited at 700 ^oC on r-cut sapphire, B) after 1 hr annealing at 1050 ^oC, C) as deposited at 650 ^oC on (001) YSZ, D) after 1 hr annealing at 1050 ^oC. Reduction of lateral strain-like disorder broadening and diffuse scattering by the annealing is clearly evident by comparing (224) maps in panels A) and B). Here ψ is the angle

of inclination of the scattering vector S **with respect to the film normal. Dotted lines in panel B) show normal and lateral reflection width in (004) and (224) reflections. Note, that the normal width stays the same, while the lateral width significantly changes.**

Close relationship between the grain size and the RMS strain in our samples is demonstrated in Fig. 4, where we correlate the RMS lateral strain with the lateral coherence length ξ_x. The figure summarizes results of this part of the CRADA work. Data for nano-grained ceramics provided by Dr. J. Rupp[36] are also plotted as closed triangles; data on isolated nano-crystals adapted from work of Zhang et al.[31] are plotted as stars. Data for the ceramic and the nano-crystallites were calculated from powder diffraction spectra, thus representing an orientation average of the grain size and the RMS strain. These sets of data can be classified as: (i) a two-dimensional case of a film with columnar grains with free surface and vertical low-angle grain boundaries, (ii) a three-dimensional case of a bulk ceramic with interconnected high-angle grain boundaries and (iii) isolated, unsupported ceria crystallites.

Isolated ceria crystallites are practically dislocation-free, as indicated by very low level of RMS strain in these samples. Low dislocation content in sub-micron crystals is due to high surface area, which creates multiple routs for the dislocation escape and is often referred as "dislocation starvation" effect.[37] Both ceramic and film samples show high level of initial or "as grown" defects, which annihilate as the grain growth is initiated by the high-temperature annealing. The solid lines represents $\varepsilon \infty \xi^{-\alpha}$ fits, best fit exponent values being $\alpha = 0.87 \pm 0.13$ for the 20 nm ceria films and $\alpha = 2.1 \pm 0.6$ for the ceramic. The initial strain dependence on the grain size in thin films was explained by Seel et al.[38] who numerically modeled average lateral strain $< \varepsilon >$ associated with the island zipping and found that $<\varepsilon> \propto R^{-\alpha}$, where *R* is the average island radius and α is an exponent varying from 0.9 to 1.4, depending on the island-substrate contact angle. The same model predicts that the grain boundary zipping would produce normal strain less than 5% of the lateral component, in agreement with the absence of ε_{zz} RMS strain. We conclude that dependence of the initial RMS strain on the lateral grain in as-deposited films can be accounted by dislocations generated by relaxation of elastic deformation of interconnected Volmer-Weber islands. This also implies that the defect structure of these samples is dominated by the grain coalescence, rather than by the film-substrate interface. We attribute the difference in the relaxation behavior between the epitaxial films and the ceramics in Fig. 4 to higher dislocation absorption rate by high-angle grain boundaries.

Final report on CRADA: Study of the nucleation and growth of YBCO on oxide buffered metallic tapes

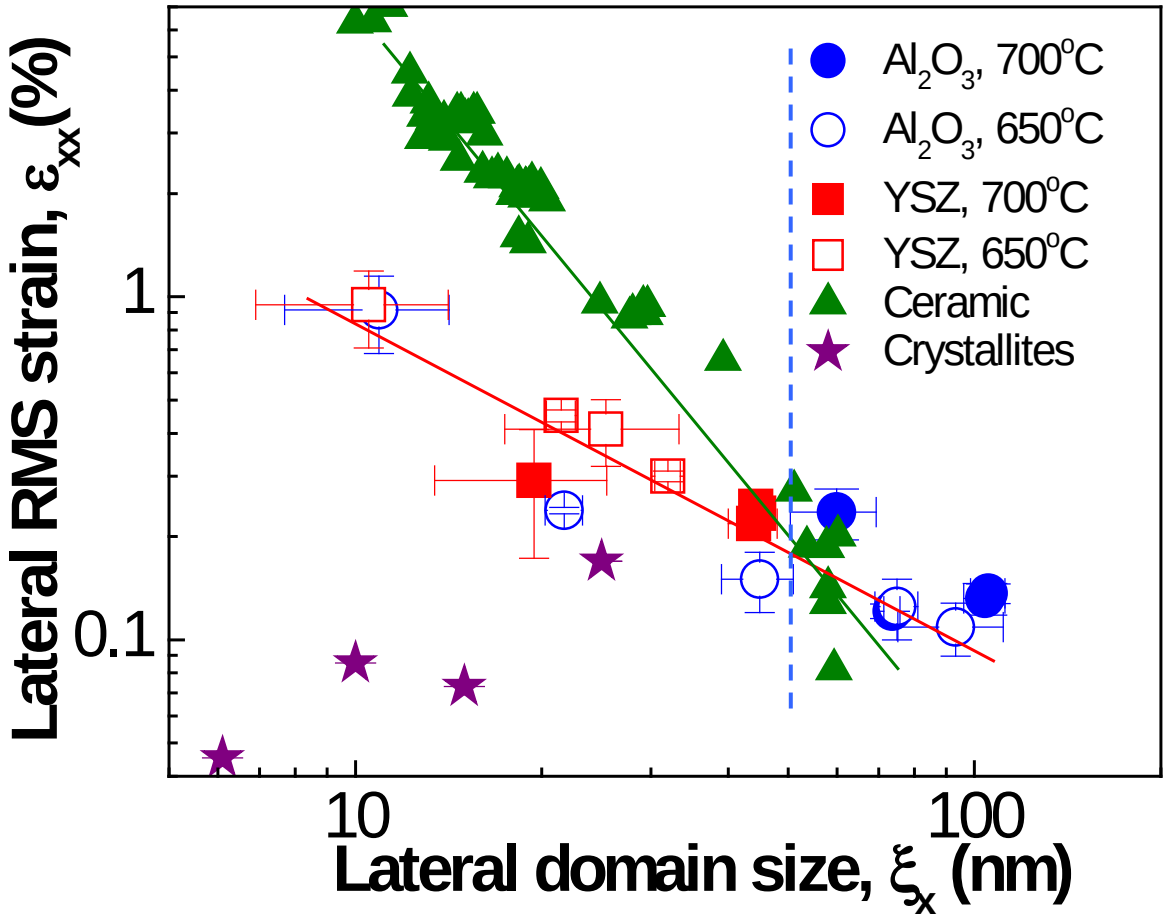

Fig. 4. Correlation of the lateral coherence length ξ_x with the lateral RMS strain ε_{xx}. The dashed vertical line is 2.5 thickness limit for the normal grain growth predicted by Mullins thermal grooving model [39]. Note that ξ_x for YSZ sample is on the left side of the line. Filled triangles are data on bulk ceramics, digital data kindly provided by Dr. J. Rupp,[36] and stars are data on isolated nano-crystals adapted from Zhang et.al.[31] For these datasets the RMS strain and the grain size values were derived from powder diffraction spectra. The solid lines are $\varepsilon \propto \xi^{-\alpha}$ fits, α = 0.87 ± 0.13 for the films and α = 2.1 ± 0.06 for the ceramic.

Final report on CRADA: Study of the nucleation and growth of YBCO on oxide buffered metallic tapes

b. Study of YBCO nucleation on "model" ceria buffers and on RABiTS.

MOD precursor films were deposited on ceria buffers at American Superconductor Corporation, Devens, MA. The precursor films had stoichiometric ratio of Y:Ba:Cu with 50% excess of Dy [40]; the inductive coupled plasma analysis confirmed that the fully converted films had the composition within 5% of the target. The MOD precursor layers were deposited on two kinds of substrates.

The structure of the film at the early stages of nucleation and growth was studied at X-18A beamline, National Synchrotron Light Source (NSLS). The X-ray radiation exited from a bending magnet section of the synchrotron ring. A channel-cut Si (111) monochromator selected a monochromatic portion of the X-ray beam (10 kV, $4x10^{-4}$ spectral width) which was focused by a Kirpatrick-Baetz mirror into a 1 mm spot at the sample, delivering total flux up to 10^{11} photons/sec. In the following discussion the peak positions were converted to equivalent 2θ values corresponding to CuKα_1 radiation for easy comparison with a sealed source (X-ray tube) results. Higher energy (10.00 kV vs. 8.05 kV for CuKα1) was chosen to attain better penetration of X-rays through the un-reacted precursor film. X-18A beamline delivered approximately two orders of magnitude higher intensity compared with a typical 1.5 kW tube source. Additionally, X-18A uses monochromatic radiation which is combined with higher angular resolution, while the tube source resolution is limited by Cu Kα_1-Kα_2 doublet. Fig. 5 compares spectra of 1.2 μm MOD film on RABiTS tape at the initial stage of nucleation recorded at X-18A and Phillips Bragg-Brentano diffractometer with 1.5 kW sealed source. The YBCO nucleation event is detected by appearance of weak YBCO peaks at $2\theta \approx 7.5^{o}$, and 46^{o}, corresponding to (001) and (006) reflections of bulk YBCO (there is an additional low-intensity peak at 23^{o}, possibly YBCO (003)). These reflections are well resolved in the lower spectrum in Fig. 5 and are completely absent from the spectrum acquired using the sealed tube source. Fig. 5 also shows that the beamline offers better resolution for polycrystalline reflections of the precursor (mostly barium oxy-fluoride and copper oxide in this sample) and Ni-W base surface oxidation (nickel oxide peaks).

Final report on CRADA: Study of the nucleation and growth of YBCO on oxide buffered metallic tapes

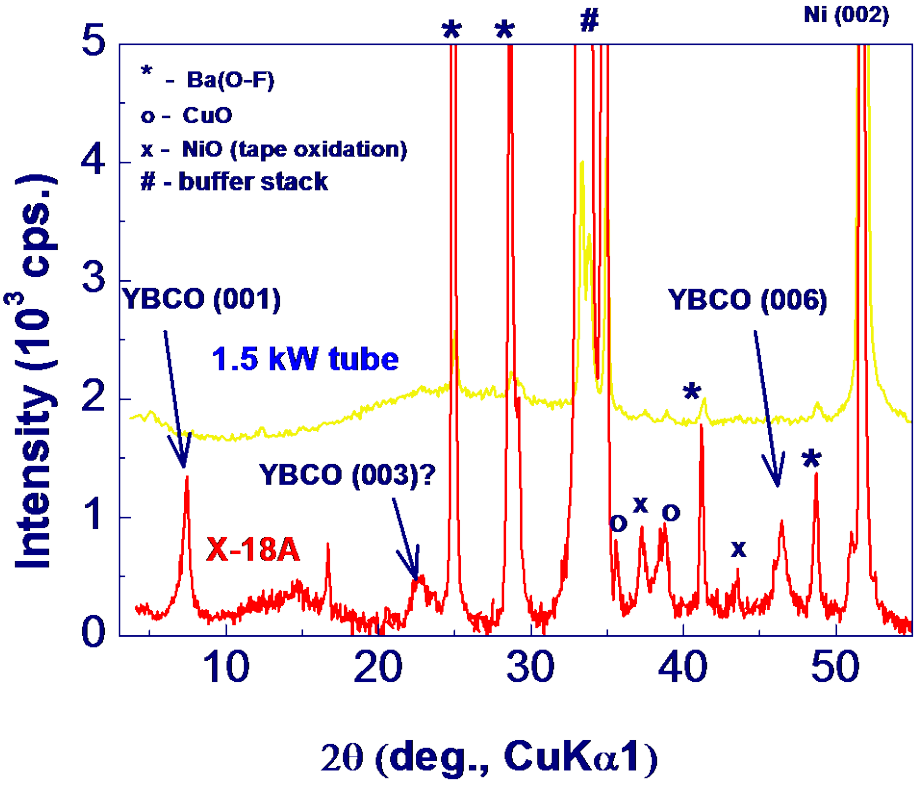

Fig. 5. Comparison of 2θ spectra of partially-processed 1.2 μm MOD sample recorded on Phillips Bragg-Brentano diffractometer with 1.5 kW Cu source (upper curve) and X-18A NSLS beamline (lower curve). Note that the YBCO nuclei peaks at $2\theta \approx 7.5^{o}$ (001) and 46.5^{o} (006) completely disappears when the sealed source is used. The 2θ angle values in the X-18A spectrum were converted to CuKα1 equivalent.

To understand role of the buffer surface we compare YBCO formation on "model" ceria buffers deposited on single-crystalline substrates with the RABiTS tapes. Ideal flatness and excellent alignment of the crystal substrates allowed for unambiguous characterization of the ceria buffer and epitaxial YBCO layer by means of X-ray reciprocal space mapping and real space (atomic force microscopy) imaging. This is difficult to do with modern 2G wire templates which incorporate three oxide layers [7] deposited on a fairly mis-oriented ($<5^{o}$) Ni-W metal base. By changing the deposition temperature and duration of post-processing, we vary the model ceria buffer quality from a very small-grained, highly defective film to a layer with single crystalline quality and very large ceria terminations. X-ray diffraction analysis shows that all model buffers have the normal correlation length ξ_z equal to the film thickness and the normal RMS strain $<\varepsilon_{zz}>$ to be less than 0.1%. No appreciable homogeneous strain was detected; full homogenous strain relaxation is indeed expected for this kind of films from minimization of elastic energy argument [41]. As the lateral correlation length ξ_x changed from 10 to 100 nm as the result of

post-annealing, the lateral RMS strain $<\varepsilon_{xx}>$ fell from 1% for a sample with $\xi_x \approx 10$ nm to 0.1% for a sample with $\xi_x \approx 100$ nm, Fig. 7. The changes in the lateral correlation lengths are a consequence of purely lateral growth of some of the grains consuming neighboring grain by normal or abnormal mechanism [42]. The same grain growth process reduces the RMS strain of the buffer. The lateral RMS strain, $<\varepsilon_{xx}>$, is a measure of amplitude of inhomogeneous deformation in the lateral (parallel to the film surface) direction. The primary sources of such a strain are most likely dislocations with the Burgers vector parallel to the film face. Reduction of lateral RMS strain during the grain growth is most likely a consequence of the dislocation annihilation. Fig. 6A summarizes the X-ray diffraction results in a structure model of these buffers: the ceria films are comprised of columnar grains, where the grain height was equal to the film thickness, 20 nm, and the average lateral grain diameter changed from 10 to 100 nm. Fig. 6B compares rocking curves of the (002) ceria buffer reflection and that one of the (003) reflection of 1.2 μm YBCO film epitaxially grown on this buffer. The comparison demonstrates that in this case, misorientation of the substrate is minor contribution to the YBCO film texture quality, which is determined by intrinsic factors, such as YBCO nuclei misorientation.

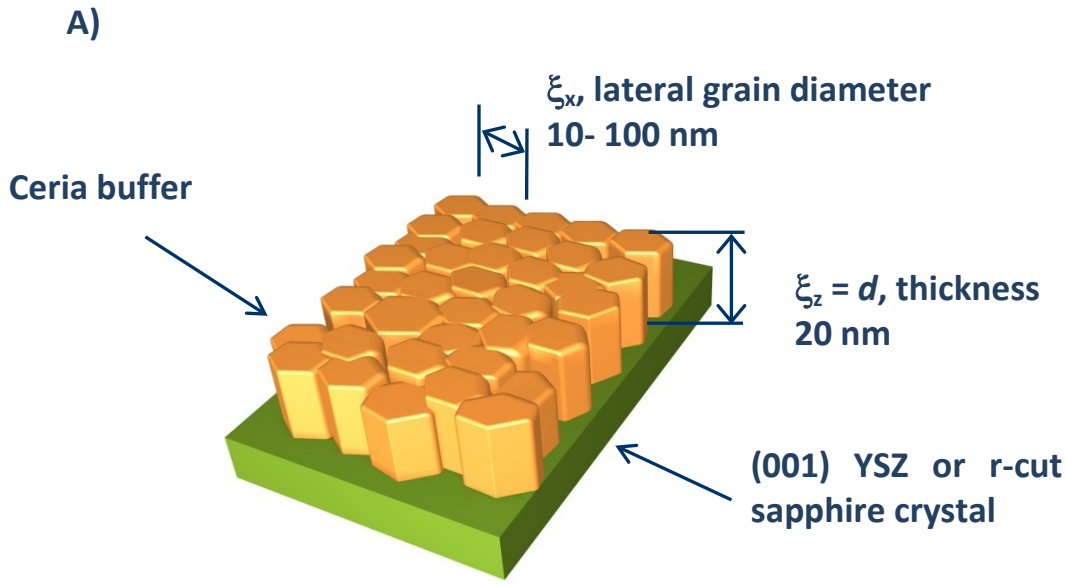

Final report on CRADA: Study of the nucleation and growth of YBCO on oxide buffered metallic tapes

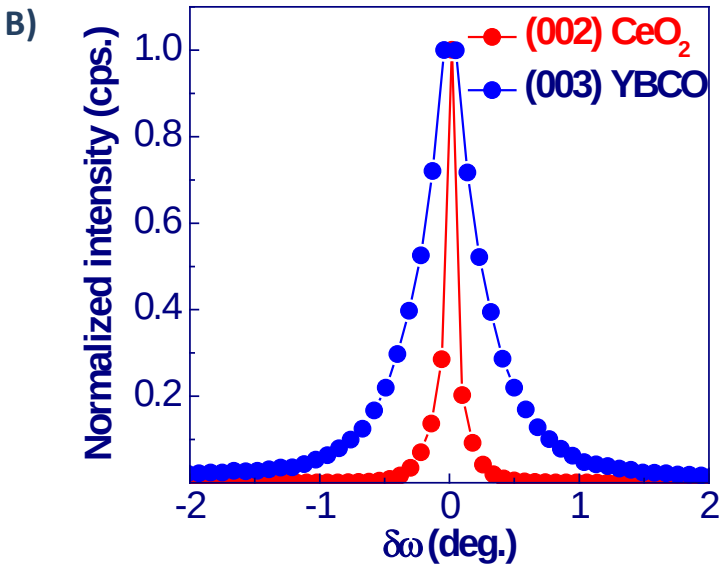

Fig. 6. A) Schematic illustration of the model ceria buffer structure: a columnar film ceria film deposited on a single-crystalline substrate. The lateral grain size was varied from 10 to 100 nm, while the normal grain size stayed constant, 20 nm B) Comparison of ω-scans of (002) CeO_2 substrate (FHWM = 0.05°) and (003) YBCO film (FWHM = 0.48°) reflections demonstrates that the YBCO film texture is dominated by intrinsic factors and not by the substrate misalignment.

The right panel in Fig. 7 presents three optical micrographs of 1.2 μm YBCO precursor films deposited on corresponding ceria buffers (solid arrows associate the micrographs and their data points) after 10% conversion at 0.6 nm/s YBCO growth rate. The YBCO grains can be easily detected as dark disks imbedded in unreacted precursor, which appear white. Our earlier TEM study [23] of similar samples has shown that the disk-shaped features, visible in optical micrographs in Fig. 7 are single YBCO grains. Since the YBCO grains had not yet coalesced at this point of processing, the number of grains is equal to the number of YBCO nuclei. We observe that the YBCO nuclei become denser as the ceria buffer grain size (determined by X-ray diffraction) increases from the smallest value of 10 nm (sample *SC1*) to approximately 20 nm (sample *SC2*). However, as the ceria grains become larger than 30 nm, the nuclei density starts to fall (sample *SC3*), becoming almost zero for ceria buffers with 100 nm grains.

We selected three samples for detailed synchrotron X-ray diffraction study of YBCO formation on model ceria buffers with varying lateral grain size and on long-length RABiTS tape. The YBCO precursor layer was deposited on a small-grain $\xi_x = 20 \pm 1$ nm buffer, labeled *SC2* in Fig. 7; one with larger grains, $\xi_x = 80 \pm 4$ nm, labeled *SC3* in a RABiTS tape coupon (sample *R* in

Final report on CRADA: Study of the nucleation and growth of YBCO on oxide buffered metallic tapes

the following). We observe approximately 5 times higher YBCO nuclei density on the sample *SC2* as compared with the sample *SC3* under identical processing conditions and 10 times higher nuclei density compared with the RABiTS sample *R*. We excluded sample *SC1* from the analysis, because due to very slow nucleation of c-axis YBCO on *SC1* substrate, the completely processed YBCO layer contained significant amount of randomly oriented YBCO.

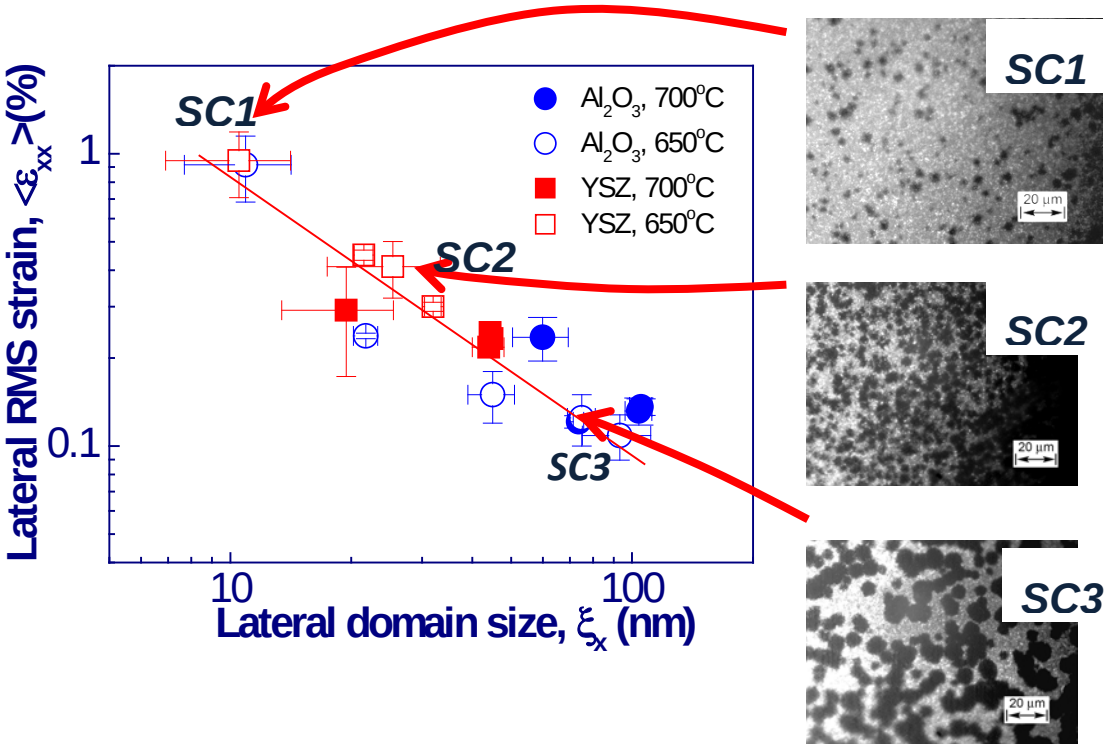

Fig. 7. Relationship between the lateral grain size and lateral RMS strain of 20 nm (001) ceria films deposited on (001) YSZ and r-cut sapphire. On the right panel are three optical micrographs of 1.2 μm YBCO films deposited on corresponding ceria buffers (indicated by arrows) and processed for 1 min at 0.6 nm/s. YBCO grains are visible as black disks embedded in lighter precursor. The highest density of YBCO nuclei is achieved at approximately 20 nm ceria grain size, sample *SC2*.

In this section we first use synchrotron radiation to examine phase evolution in the RABiTS sample *R* then compare it with the two model buffer samples, *SC2* and *SC3*, processed under identical conditions. Fig. 8 presents 2θ diffraction spectra (CuKα1 equivalent angles) of

the RABiTS sample in the precursor state (panel A), immediately after the nucleation event becomes detectable by XRD (panel B), after 10% processing time (panel C) and after complete processing and oxygenation (panel D). The spectrum of the precursor films contains well-recognizable reflections of barium oxy-fluoride (structurally very similar to barium fluoride) and copper oxide. The YBCO nucleation becomes first detectable after 3 min as appearance of (001) and (006) reflections. During further processing we observe disproportionate enhancement of (001) intensity and gradual development of (003), (005) and (007) reflections, panel C. Notably, (002) reflection is the last to develop. After 10% processing $Y_2Cu_2O_5$ phase starts to form as evidenced by emergence of a new peak at $2\theta = 31.8^o$, indentified as (211) reflection $Y_2Cu_2O_5$ phase, panel C. Another event, occurring at 10% processing, is broadening of the precursor reflections at $2\theta \approx 29^o$ and $2\theta \approx 25^o$. This is explained by simultaneous ordering of oxygen and fluorine in the precursor formation of secondary phases, such as Dy_2O_3, Y_2O_3 and $BaCuO_2$ [43-44]. Due to overlapping of these peaks, positive phase identification could not be made. After complete conversion, panel *D*, the sample is c-axis oriented YBCO film, with strong reflections at 29^o, $BaCuO_2$ being the only detectable impurity phase. The NiO (002) reflection at 43^o becomes much stronger due to oxidation of the Ni-W tape during the processing.

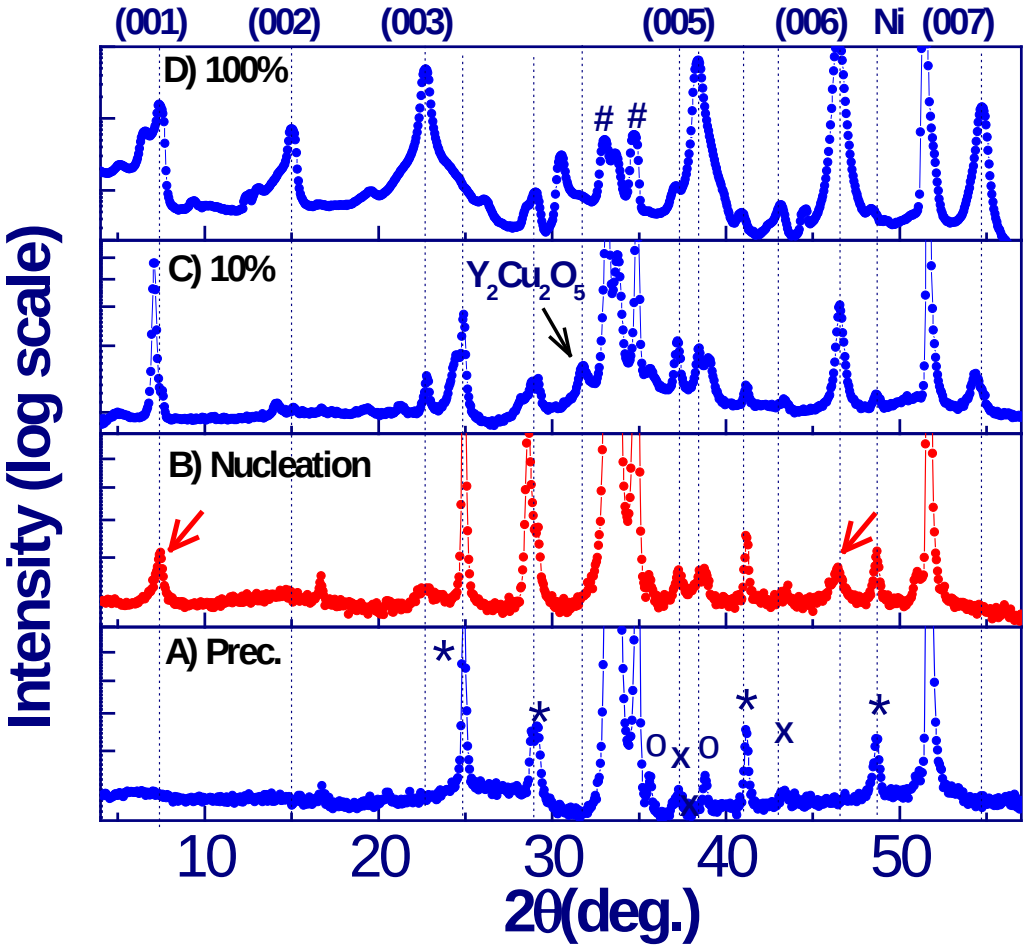

Fig. 8. Evolution of 2θ spectra of 1.2 μm YBCO film on RABiTS. "Snapshots" during processing at 0.6 nm/s are: A) precursor, B) start of YBCO nucleation, C) after 10% of conversion time passed and C) complete conversion. Positions of the (00l) YBCO reflections are indicated by the vertical dashed lines, * marks Ba(O-F) reflections, o - indicates CuO, x - NiO and # labels the buffer stack reflections. The nucleation event is detected by appearance of peaks at $2\theta \approx 7.5^{o}$ and 46.4^{o}, corresponding to (001) and (006) reflections of bulk YBCO, respectively. Both peaks are indicated by arrows. After 10% of the processing time passed a secondary phase, $Y_2Cu_2O_5$ (indicated by an arrow in panel C) starts to form. The 2θ angle values were converted to CuKα1 equivalent.

In the next set of experiments we aimed to establish whether phase evolution, shown in Fig. 8 can be influenced by changing morphology of the ceria template. The optical micrographs in Fig. 7 suggest the YBCO nuclei density is strongly affected by the lateral grains size and RMS strain of the ceria layer. Since In Fig. 9 we compare 2-θ X-ray diffraction spectra of the three samples at nucleation stage (panel A) and after 1 min of processing at 0.6 mn/s (panel B). Solid lines approximate the detectable YBCO peaks, the rest of the peaks are indentified as the substrate or the precursor reflections. The spectra of the nucleation stage, Fig. 9A, emphasize that the substrate structure has strong influence on the structure of the epitaxial YBCO at the early stage of the film formation. The film on the RABiTS tape nucleates as a disordered phase with only (001) peak detectable. Notably, it takes 3-4 minutes for the peak to appear after the processing temperature reaches the pre-set value of 780°C. In contrast, YBCO forms practically instantly on model buffer substrate. Only film on the small-grain substrate develops all the (00*l*) reflections characteristic of c-axis oriented YBCO right from the onset of the processing. The film on the large-grain substrate forms an intermediate phase with (006) reflection being the only detectable (00*l*) peak. This intermediate layer is very thin (<10 nm) as can be inferred from very large width of the peak.

After 10% of the processing time passed, the structure of YBCO on model substrate becomes well-defined c-axis oriented YBCO. The *SC2* sample exhibits the fastest formation of YBCO layer, which can be recognized by sharp and narrow (00*l*) peaks. The line broadening analysis confirms that the thickness of the YBCO layer on *SC2* substrate is approximately 100 nm, as expected from the processing time estimate. In contrast, YBCO on *SC3* substrate demonstrates slower growth, in the same time span the film thickness is only 50 nm. Low intensity of (002) YBCO peak of the *R* sample indicates significant amount of disorder still present in this sample even after 10% conversion. Notably, both *R* and *SC3* samples show signs of barium oxy-fluoride superstructure formation [44], indicated by either splitting (*SC3* sample) or broadening of (111) reflection at $2\theta = 25^{o}$. In contrast, in sample *SC2* the precursor structure does not change during the growth. The narrow precursor reflections which maintain the position throughout the processing suggest no precursor ordering.

Final report on CRADA: Study of the nucleation and growth of YBCO on oxide buffered metallic tapes

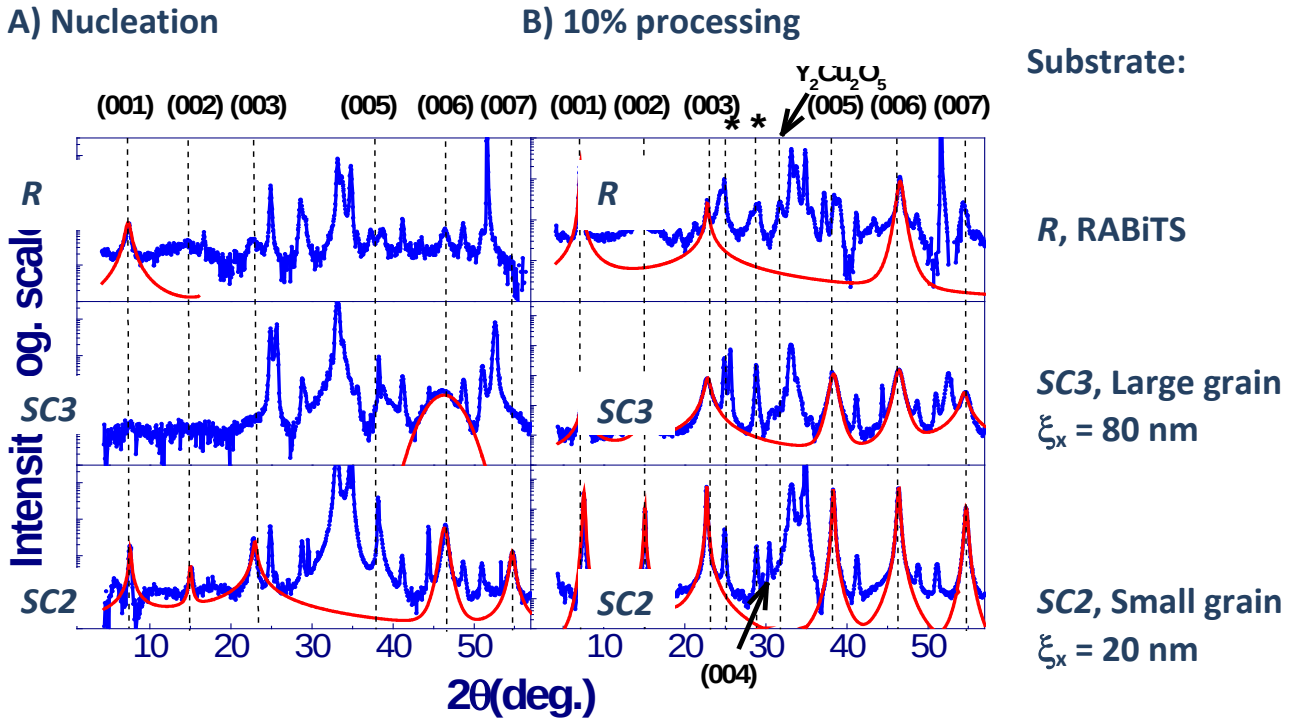

Fig. 9. Evolution of the 2-θ diffraction spectra of 1.2 μm precursor films deposited on the following substrates: (i) RABiTS tape (sample *R*), (ii) CeO_2 buffer with 80 nm average ceria grain size (sample *SC3*, refer to Fig. 7); CeO_2 buffer with 20 nm grain size (sample *SC2*, refer to Fig. 7). Panel A) shows the spectra immediately after the nucleation event, and panel B) after 10% conversion. Solid lines are pseudo-Voight approximations of (00l) YBCO reflections which emphasize the difference in the early YBCO structure development between these substrates.

1.4. Unresolved challenges encountered in the work

In the CRADA work we extensively used X-ray reflectivity to determine density and roughness of ceria buffers deposited on very flat single-crystalline substrates. X-ray reflectivity cannot be applied to measure a film density on a non-flat substrate, such a metal foil, because significant broadening of the specular reflection prevents precise analysis of the reflectivity

profile. An alternative method, such as Rutherford backscattering might provide important information on the ceria buffer density in RABiTS tapes. In the future research we plan to investigate influence of the ceria buffer density of nucleation kinetics.

The grain size and strain analysis of ceria on RABiTS can be performed using X-ray micro-beam. We tried several experiments using X-13A beamline at NSLS. While reciprocal maps could be recorded, there was significant instrumental broadening at the high end of the spectrum, 20kV, which prevented us getting reliable data. We expect that more advanced light sources, such as NSLS-II, will make such experiments possible in the near future.

1.5. Roles and Responsibilities

c. Brookhaven National Laboratory team

Brookhaven team was responsible for processing precursor samples deposited ceria buffers and characterization of the films by X-ray diffraction and electron microscopy. BNL team was also responsible for writing and submission of facility proposals (CFN and NSLS), preparation of scientific publications and reporting of the results at scientific meetings and annual DOE program peer reviews at Washington, DC.

d. American Superconductor Corp. team

AMSC team was responsible for deposition of the industrial precursor films using proprietary sol-gel technology similar to one used in the large-scale production of 2G wires. Overall in the course of the CRADA over 50 samples were made and characterized.

2. Summary of CRADA results

1. The average lateral grain size of (001) ceria was found to be inversely proportional to the lateral RMS strain. After isothermal annealing, films on r-cut sapphire exhibited faster grain growth and better structural quality than identical films deposited on (001) YSZ. We ascribe the difference to the onset of abnormal grain growth, which arises due to large fluctuation of the initial grain size in the films on r-cut sapphire. The non-uniform grain size distribution is corroborated by AFM surface profile and rocking curve analysis. The effect is suppressed by a 2.2^{o} miscut due to monomodal grain size distribution in a miscut sample. The result emphasizes negative effect of the out-of-plane tilt on the nucleation kinetics.

2. The best-performing MOD YBCO layers are those that immediately form ordered orthorhombic YBCO after the temperature ramp-up. Rate of YBCO nucleation and structure of the nuclei are influenced by fine details of ceria buffer surface, such as lateral grain size and lateral RMS strain. Surprisingly, ceria buffers with single-crystal like quality are not the best substrates for MOD YBCO growth. Nucleation of YBCO is substantially assisted by special nucleation centers, most likely outcrops of threading dislocations. We also note that development of the transient and secondary phases in the precursor is strongly affected by the substrate activity. A substrate that promotes a high rate of YBCO nucleation also maintains the precursor structure with minimum secondary phase formation and precursor ordering. An

important factor, not addressed into our analysis, is density of the buffer. A porous buffer would allow dislocations to annihilate during the post annealing, thus dramatically reducing density of the nucleation centers even in a buffer with optimum grain size.

3. Future work

Epitaxy on optimally strained (001) ceria substrates made in the course of the CRADA produced a new type of structural order: a long-period (17 nm) superstucture.

The superstructure is observed as two peaks in the diffraction spectrum, Fig. 10.

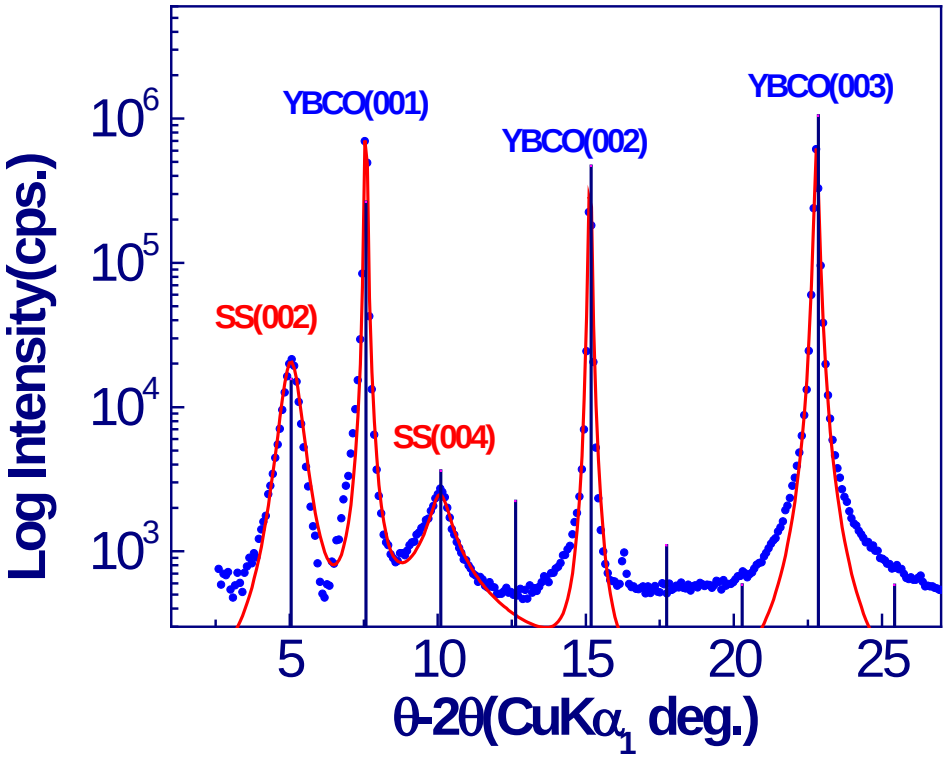

Fig. 10. X-ray diffraction spectrum of YBCO film showing the additional superstructure peaks corresponding to lattice spacing 1.74 and 0.88 nm. The solid lines are Pseodo-Voight approximations used in the line shape analysis. The vertical bars represent position and relative intensity of (00l) peaks of a model structure shown in Fig. 11. The spectrum was acquired using 10 kV synchrotron radiation.

The superstructure formation is explained by normal oxygen ordering in Cu-O chains, Fig. 11.

Final report on CRADA: Study of the nucleation and growth of YBCO on oxide buffered metallic tapes

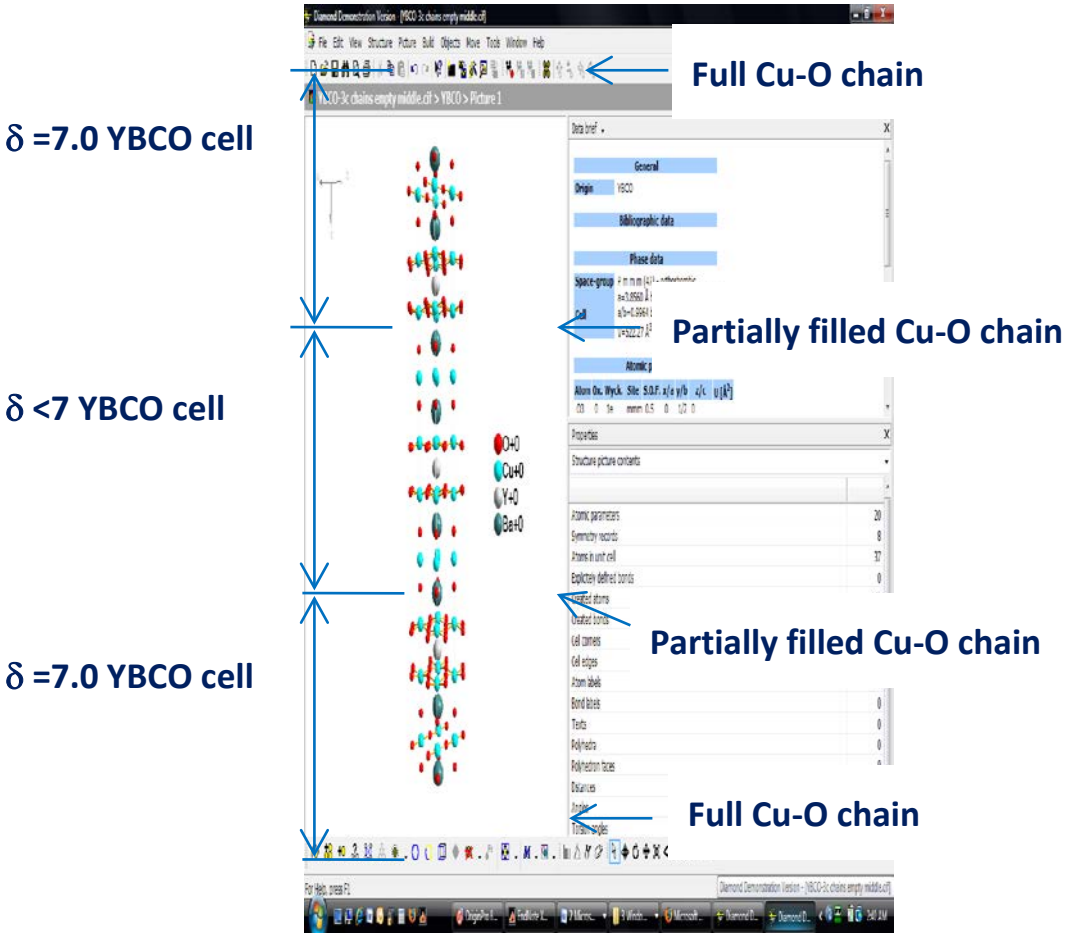

Fig. 11. Crystallographic model of (00l) oxygen vacancy ordering. The diagram shows a sequence of two stoichiometric (δ=7) YBCO cells with partially filled one (δ<7) in the middle. The super-cell is has chemical formula $Y_3Ba_6Cu_9O_{18.5}$ and has c-axis lattice parameter of 3.5 nm. This model explains extra peaks at 2θ = 5° and 10°, Fig. 10 as (002) and (004) superstructure reflections.

Samples with well-developed superstructure exhibit very high critical current density and low flux creep rate, which opens a possibility for design of high-performance material for 2G wire.

4. References

[1]. Maiorov B, Baily S A, Zhou H, Ugurlu O, Kennison J A, Dowden P C, Holesinger T G, Foltyn S R, and Civale L, "Synergetic combination of different types of defect to optimize pinning landscape using BaZrO3-doped YBa2Cu3O7", *Nat Mater*, 8 (2009), pp: 398-404.

Final report on CRADA: Study of the nucleation and growth of YBCO on oxide buffered metallic tapes

[2]. Aytug T, Paranthaman M, Leonard K J, Kim K, Ijaduola A O, Zhang Y, Tuncer E, Thompson J R, and Christen D K, "Enhanced flux pinning and critical currents in YBa[sub 2]Cu[sub 3]O[sub 7 - delta] films by nanoparticle surface decoration: Extension to coated conductor templates", *Journal of Applied Physics*, 104 (2008), pp: 043906-043906.

[3]. Wang H, Liao X Z, Xu H F, Zhang X, Lin Y, Foltyn S R, Arendt P N, MacManus-Driscoll J L, Zhu Y T, and Jia Q X, "Effects of Eu interfacial mobility on the growth of epitaxial EuBa2Cu3O7-delta films", *Applied Physics Letters*, 86 (2005), pp: -.

[4]. Gutierrez J, Llordes A, Gazquez J, Gibert M, Roma N, Ricart S, Pomar A, Sandiumenge F, Mestres N, Puig T, and Obradors X, "Strong isotropic flux pinning in solution-derived YBa2Cu3O7-x nanocomposite superconductor films", *Nature Materials*, 6 (2007), pp: 367-373.

[5]. Puig T, Gutierrez J, Pomar A, Llord, s A, zquez J, Ricart S, Sandiumenge F, and Obradors X, "Vortex pinning in chemical solution nanostructured YBCO films", *Superconductor Science and Technology*, 21 (2008), pp: 034008.

[6]. Zhou H, Maiorov B, Baily S A, Dowden P C, Kennison J A, Stan L, Holesinger T G, Jia Q X, Foltyn S R, and Civale L, "Thickness dependence of critical current density in YBa2Cu3O7−δ films with BaZrO3 and Y2O3 addition", *Superconductor Science and Technology*, 22 (2009), pp: 085013.

[7]. Rupich M W, Zhang W, Li X, Kodenkandath T, Verebelyi D T, Schoop U, Thieme C, Teplitsky M, Lynch J, Nguyen N, Siegal E, Scudiere J, Maroni V, Venkataraman K, Miller D, and Holesinger T G, "Progress on MOD/RABiTSTM 2G HTS wire", *Physica C*, 412-414 (2004), pp: 877-884.

[8]. Teranishi R, Matsuda J, Nakaoka K, Fuji H, Aoki Y, Kitoh Y, Nomoto S, Yamada Y, Yajima A, Izumi T, and Shiohara Y, "High-Ic processing for YBCO coated conductors by TFA-MOD process", *Physica C: Superconductivity*, 426-431 (2005), pp: 959-965.

[9]. Izumi T, Tokunaga Y, Fuji H, Teranishi R, Matsuda J, Asada S, Honjo T, Shiohara Y, Muroga T I, Miyata S, Watanabe T, Yamada Y, Iijima Y, Saitoh T, Goto T, Yoshinaka A, and Yajima A, "Progress in development of coated conductors by TFA-MOD processing", *Physica C-Superconductivity and Its Applications*, 412-14 (2004), pp: 885-889.

[10]. Holesinger T G, Civale L, Maiorov B, Feldmann D M, Coulter J Y, Miller D J, Maroni V A, Chen Z, Larbalestier D C, Feenstra R, Li X, Huang Y, Kodenkandath T, Zhang W, Rupich M W, and Malozemoff A P, "Progress in Nanoengineered Microstructures for Tunable High-Current, High-Temperature Superconducting Wires", *Advanced Materials*, 20 (2008), pp: 391-407.

[11]. Gazquez J, Sandiumenge F, Coll M, Pomar A, Mestres N, Puig T, Obradors X, Kihn Y, Casanove M J, and Ballesteros C, "Precursor evolution and nucleation mechanism of YBa2Cu3Ox films by TFA metal-organic decomposition", *Chemistry of Materials*, 18 (2006), pp: 6211-6219.

[12]. Pinol S, and Castano O, "Water vapour pressure influence on the kinetics of the superconducting YBCO thin films epitaxic growth by the TFA-MOD method", *Physica C-Superconductivity and Its Applications*, 450 (2006), pp: 48-55.

[13]. Feenstra R, Lindemer T B, Budai J D, and Galloway M D, "Effect of Oxygen-Pressure on the Synthesis of Yba2cu3o7-X Thin-Films by Postdeposition Annealing", *Journal of Applied Physics*, 69 (1991), pp: 6569-6585.

[14]. Honjo T, Nakamura Y, Teranishi R, Fuji H, Shibata J, Izumi T, and Shiohara Y, "Growth mechanism of YBCO films in metal organic deposition method using trifluoroacetates", *Ieee Transactions on Applied Superconductivity*, 13 (2003), pp: 2516-2519.

[15]. Feenstra R, Gapud A A, List F A, Specht E D, Christen D K, Holesinger T G, and Feldmann D A, "Critical currents I-c(77 k) > 350 A/cm-width achieved in ex situ YBCO coated conductors using a faster conversion process", *Ieee Transactions on Applied Superconductivity*, 15 (2005), pp: 2803-2807.

[16]. Wesolowski D E, Yoshizumi M, and Cima M J, "Trajectory-property relationships in MOD-derived YBCO films", *Physica C-Superconductivity and Its Applications*, 450 (2006), pp: 76-82.

[17]. Yoshizumi M, Seleznev I, and Cima M J, "Reactions of oxyfluoride precursors for the preparation of barium yttrium cuprate films", *Physica C-Superconductivity and Its Applications*, 403 (2004), pp: 191-199.

[18]. Matsuda J, Nakaoka K, Izumi T, Yamada Y, and Shiohara Y, "Microstructure evolution of YBCO films deposited by advanced TFA-MOD process", *Physica C: Superconductivity*, 468 (2008), pp: 1017-1023.

[19]. Solovyov V F, Wiesmann H J, and Suenaga M, "Critical current densities and the structural quality of 3- and 4-mu m-thick superconducting $YBa_2Cu_3O_7$ layers synthesized using the ex situ process", *Journal of Applied Physics*, 102 (2007), pp: 053902-053908.

[20]. Skårman B, Wallenberg L R, Larsson P-O, Andersson A, Bovin J-O, Jacobsen S N, and Helmersson U, "Carbon Monoxide Oxidation on Copper Oxide Thin Films Supported on Corrugated Cerium Dioxide {111} and {001} Surfaces", *Journal of Catalysis*, 181 (1999), pp: 6-15.

[21]. Costa-Nunes O, Gorte R J, and Vohs J M, "Comparison of the performance of Cu-CeO2-YSZ and Ni-YSZ composite SOFC anodes with H2, CO, and syngas", *Journal of Power Sources*, 141 (2005), pp: 241-249.

[22]. Steele B C H, and Heinzel A, "Materials for fuel-cell technologies", *Nature*, 414 (2001), pp: 345-352.

[23]. Solovyov V F, Li Q, Wiesmann H, Oleynikov P, and Zhu Y, "Strong influence of the $YBa_2Cu_3O_7$ grain size on critical current densities of thick $YBa_2Cu_3O_7$ layers made by a metal-organic deposition process", *Superconductor Science and Technology*, 21 (2008), pp: 125013.

[24]. Baudin M, Wójcik M, and Hermansson K, "Dynamics, structure and energetics of the (111), (011) and (001) surfaces of ceria", *Surface Science*, 468 (2000), pp: 51-61.

[25]. Sayle D C, Sayle T X T, Parker S C, Catlow C R A, and Harding J H, "Effect of defects on the stability of heteroepitaxial ceramic interfaces studied by computer simulation", *Physical Review B*, 50 (1994), pp: 14498.

[26]. Herman G S, "Surface structure determination of CeO2(001) by angle-resolved mass spectroscopy of recoiled ions", *Physical Review B*, 59 (1999), pp: 14899.

[27]. Cabrera N, "The equilibrium of crystal surfaces", *Surface Science*, 2 (1964), pp: 320-345.

[28]. Herring C, "Some Theorems on the Free Energies of Crystal Surfaces", *Physical Review*, 82 (1951), pp: 87.

[29]. Wang Z L, and Feng X, "Polyhedral Shapes of CeO2 Nanoparticles", *Journal of Physical Chemistry B*, 107 (2003), pp: 13563-13566.

[30]. Marks L D, "Particle size effects on Wulff constructions", *Surface Science*, 150 (1985), pp: 358-366.

[31]. Zhang F, Jin Q, and Chan S-W, "Ceria nanoparticles: Size, size distribution, and shape", *Journal of Applied Physics*, 95 (2004), pp: 4319-4326.

[32]. Jacobsen S N, Helmersson U, Erlandsson R, Skarman B, and Wallenberg L R, "Sharp microfaceting of (001)-oriented cerium dioxide thin films and the effect of annealing on surface morphology", *Surface Science*, 429 (1999), pp: 22-33.

[33]. Wu F, Pavlovska A, Smith D J, Culbertson R J, Wilkens B J, and Bauer E, "Growth and structure of epitaxial CeO2 films on yttria-stabilized ZrO2", *Thin Solid Films*, 516 (2008), pp: 4908-4914.

[34]. Spanková M, Vávra I, Gazi S, Machajdík D, Chromik S, Fröhlich K, Hellemans L, and Benacka S, "Growth and recrystallization of CeO2 thin films deposited on R-plane sapphire by off-axis RF sputtering", *Journal of Crystal Growth*, 218 (2000), pp: 287-293.

[35]. Develos-Bagarinao K, Yamasaki H, Nakagawa Y, Nie J C, Sohma M, and Kumagai T, "Comparative studies of nanostructural and morphological evolution of CeO2 thin films induced by high-temperature annealing", *Nanotechnology*, 18 (2007), pp: 1-9.

[36]. Rupp J L M, Infortuna A, and Gauckler L J, "Microstrain and self-limited grain growth in nanocrystalline ceria ceramics", *Acta Materialia*, 54 (2006), pp: 1721–1730.

[37]. Greer J R, Oliver W C, and Nix W D, "Size dependence of mechanical properties of gold at the micron scale in the absence of strain gradients", *Acta Materialia*, 53 (2005), pp: 1821-1830.

[38]. Seel S C, and Thompson C V, "Tensile stress generation during island coalescence for variable island-substrate contact angle", *Journal of Applied Physics*, 93 (2003), pp: 9038-9042.

[39]. Mullins W W, "The effect of thermal grooving on grain boundary motion", *Acta Metallurgica*, 6 (1958), pp: 414-427.

[40]. Rupich M W, Verebelyi D T, Zhang W, Kodenkandath T, and Li X P, *MRS Bulletin*, 29 (2004), pp: 572.

[41]. Matthews J W, and Blakeslee A E, "Defects in epitaxial multilayers: I. Misfit dislocations", *Journal of Crystal Growth*, 27 (1974), pp: 118-125.

[42]. Thompson C V, "Grain growth in thin films", *Annual Review of Materials Science*, 20 (1990), pp: 245.

Final report on CRADA: Study of the nucleation and growth of YBCO on oxide buffered metallic tapes

[43]. Wong-Ng W, Levin I, Otani M, Vaudin M D, Cook L P, Cline J, Feenstra R, and Holesinger T, "Phase relations in the Ba-Y-Cu-O films on SrTiO3 for the ex situ BaF2 process", *Applied Physics Letters*, 90 (2007), pp: -.

[44]. Wong-Ng W, Levin I, Cook L P, and Feenstra R, "Nature of the transient BaF2-related phases in the "BaF2" processing of Ba2YCu3O7-x superconductors", *Applied Physics Letters*, 88 (2006), pp: -.

5. List of figures

Final report on CRADA: Study of the nucleation and growth of YBCO on oxide buffered metallic tapes

Final report on CRADA: Study of the nucleation and growth of YBCO on oxide buffered metallic tapes

6. List of scientific papers published in the course of the CRADA

[1]. Solovyov V F, Develos-Bagarinao K, and Nykypanchuk D, "Nanoscale abnormal grain growth in (001) epitaxial ceria", *Physical Review B*, **80** (2009)**,** pp: 104102-104112.

[2]. Solovyov V F, Abraimov D, Miller D, Li Q, and Wiesmann H, "Correlation between $YBa_2Cu_3O_7$ nuclei density and the grain orientation of the CeO_2 buffered Ni--W template of the second-generation superconducting wire", *Journal of Applied Physics*, **105** (2009)**,** pp: 113927-113927.

[3]. Solovyov V F, Li Q, Wiesmann H, Oleynikov P, and Zhu Y, "Strong influence of the $YBa_2Cu_3O_7$ grain size on critical current densities of thick $YBa_2Cu_3O_7$ layers made by a metal-organic deposition process", *Superconductor Science and Technology*, **21** (2008)**,** pp: 125013.

[4]. Solovyov V F, Wiesmann H J, Wu L, Li Q, Cooley L D, Suenaga M, Maiorov B, and Civale L, "High critical currents by isotropic magnetic-flux-pinning centres in a 3 μm-thick YBa2Cu3O7 superconducting coated conductor", *Superconductor Science and Technology*, **20** (2007)**,** pp: L20-L23.

[5]. Solovyov V F, Wiesmann H J, and Suenaga M, "Critical current densities and the structural quality of 3- and 4-mu m-thick superconducting $YBa_2Cu_3O_7$ layers synthesized using the ex situ process", *Journal of Applied Physics*, **102** (2007)**,** pp: 053902-053908.

[6]. Solovyov V F, and Wiesmann H J, "Application of low-angle polishing for rapid assessment of the texture and morphology of thick film Y1Ba2Cu3O7 superconducting tapes", *Physica C: Superconductivity*, **467** (2007)**,** pp: 186-191.